



# EOR Displacement Characteristics from Cluster Analysis and Fractional Pore Occupation

Mostafa Borji<sup>1</sup> · Ahmad Kharrat<sup>1</sup> · Holger Ott<sup>1</sup> 

Received: 9 May 2023 / Accepted: 28 August 2023 / Published online: 20 September 2023  
© The Author(s) 2023

## Abstract

The in situ saponification of crude oil lowers the interfacial tensions of oil–water systems in chemical-enhanced oil recovery (cEOR). When the interfacial tension is sufficiently low, emulsion phases occur, and the fluid phase distribution in the pore space changes, affecting oil displacement efficiency. This change in capillarity allows the injection water to penetrate different classes of pores, which must be reflected in the distribution of fluids in the pore space. This issue still needs to be adequately researched and is not reflected in the classic analyses of oil cluster size. We have performed  $\mu$ CT-based coreflood experiments to study the displacement efficiency of crude oil by alkaline solutions acting as cEOR agents for in situ saponification. The measured fluid distributions were analyzed using oil-cluster size statistics. In addition, the pore classes from which the oil was preferentially displaced and the degree of displacement as a function of alkali concentration were determined. Despite ultralow interfacial tension and emulsion formation, a clear separation of the oil and aqueous phases was observed over a wide range of alkali concentrations, allowing a two-phase analysis of the microscopic fluid distribution. It was found that (a) a Lorentz analysis of the cluster volume distribution is useful to characterize the cEOR displacement efficiency. It shows the tendency of oil clusters toward a more uniform size distribution toward optimal alkali concentration. (b) the additional oil recovery toward optimal displacement conditions comes from the fraction of smaller pores; at optimal conditions, all pore classes are flooded almost equally and to a high degree, equivalent to miscible displacement, i.e., extremely low interfacial tension.

**Keywords** Alkaline flooding · In situ surfactant · Pore scale imaging · Oil cluster analysis · Pore saturation · Chemical enhanced oil recovery (EOR) · Core flooding

## 1 Introduction

Despite all efforts to realize the transition to a sustainable energy system, the demand for energy and oil is predicted to stay at a high level in the coming decades (Annual Energy Outlook 2023; Oil 2023). Conventional oil fields are often considered economically

---

✉ Holger Ott  
holger.ott@unileoben.ac.at

<sup>1</sup> Department Geoenergy, Montanuniversität Leoben, 8700 Leoben, Austria

exhausted after less than half of the oil has been produced. The remaining half can often only be extracted using special methods that require a high oil price. This leads to the need to resort to unconventional oil and gas (shale gas and oil, oil sands, etc.), whose energy and environmental performance is far worse. Alternatively, since the average recovery from conventional oil fields is on the order of 35% (Lake et al. 2014), the remaining oil can be a target for enhanced oil recovery (EOR). Alkaline flooding is an economically attractive chemical EOR method (Cooke et al. 1974; Sheng 2013; Tang et al. 2013) that can be applied in crude oils containing a high concentration of acidic components, resulting in a high total acid number (TAN) (Saha et al. 2018; She et al. 2021; Ott et al. 2020). Depending on the situation, alkaline flooding may be a standalone technology or may be combined with surfactant and polymer flooding, i.e., alkaline-surfactant-polymer (ASP) flooding (Lake et al. 2014; Sheng 2013, 2010; Ding et al. 2020; Nourani et al. 2022; Hemmati-Sarapardeh et al. 2021; Stoll et al. 2011; Ahmed and Meehan 2012). Alkaline agents are inexpensive and easy to handle. Once dissolved and dissociated in injection water, the resulting  $\text{OH}^-$  ions may saponify fatty acids at the oil–water interface, lowering the oil–water interfacial tension (Amaya et al. 2002; Chatterjee 2002; Green and Willhite 1998; Khlaifat et al. 2022; deZabala et al. 1982). From a fluid-displacement viewpoint, a system with vanishing interfacial tension starts behaving like a miscible system with a high displacement efficiency and vanishing residual saturations. However, if the interfacial tension is sufficiently low, then emulsion phases form, which generally have a higher viscosity than the liquids forming them. This may potential positive or negative effect on the displacement efficiency by entrapment of oil and microscopic sweep effects (Ott et al. 2020; Johnson 1976; Magzymov et al. 2021).

Because of the relatively high TAN values, some fields in the Vienna Basin are potential targets for alkaline flooding, and are also ideal candidates for this study because of the available data; for the present research, we chose the relevant case of the 16 TH reservoir of the Matzen Field in Austria. Experimental data on phase behavior (Magzymov et al. 2021; Borji et al. 2022; Schumi, et al. 2020) and flooding (Borji et al. 2022; Schumi, et al. 2020) are available and are compared to the present results. In this specific case,  $\text{Na}_2\text{CO}_3$  was chosen as alkali agent. Core flood experiments showed highest recovery at alkaline concentrations around  $c_{\text{Na}_2\text{CO}_3} = 7000$  to  $7500$  ppm (Borji et al. 2022; Schumi, et al. 2020), which in the following, we refer to as optimum conditions. This optimum in recovery is consistent with observed phase behavior as shown in Fig. 1 (Borji et al. 2022); in test tube experiments it has been shown that optimum  $\text{Na}_2\text{CO}_3$  concentration led to well separated and nearly unaltered oleic and aqueous phases separated by a small volume of a micro-emulsion at the interface (see Fig. 1). The mutual participation in the bulk fluid phases appeared as small. This is similar to the optimization of the injection water composition in classical surfactant flooding. While in surfactant flooding, salinity is the tuning parameter to reach optimum conditions (Winsor type III, Lake et al. 2014), in alkaline flooding, the situation is slightly more complex (Ott et al. 2020; Magzymov et al. 2021). As the alkali concentration increases, the salinity increases, but at the same time the potential for in situ generated surfactant concentration increases. For 16 TH crude oil, distinct aqueous and oleic phases were observed up to  $c_{\text{Na}_2\text{CO}_3} = 14,000$  ppm. At a much higher concentration of 24,000 ppm, a single tight (optically homogeneous) emulsion phase was observed; a “miscibility” between the fluid phases is reached by mobilizing enough surfactants from the crude oil, while at 7500 ppm, this is not the case. Also in  $\mu\text{CT}$ -based core-flood and microfluidic experiments the highest recovery factors were measured at optimal  $\text{Na}_2\text{CO}_3$  concentration. Despite the multiple contact between the oil and the alkaline solution in those experiments, a two-phase system with distinctly different fluid phases remains in the

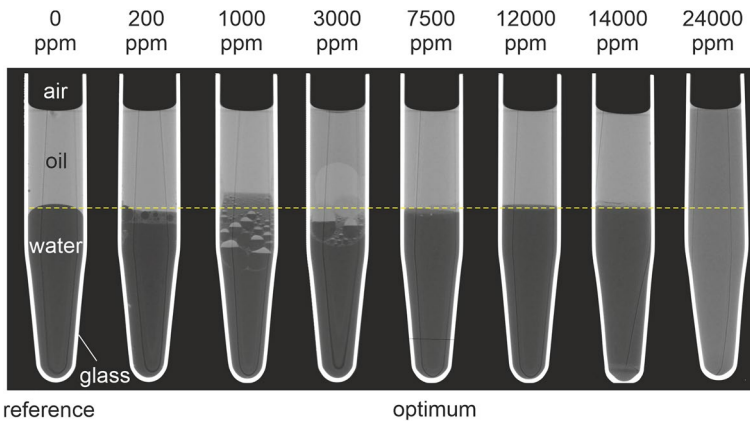


**Fig. 1** Classical test tube experiment showing the liquid distribution at equilibrium after mixing 16 TH crude oil with aqueous solutions of different  $\text{Na}_2\text{CO}_3$  concentrations between 0 and 24,000 ppm (see figure). The images were acquired with a  $\mu\text{CT}$  scanner to illustrate the X-ray contrast of the liquid phases and the structure of the loose emulsions. The yellow line shows the oil–water contact line of the reference system. Details are available in (Borji et al. 2022)

pore space as in the test tubes; a third emulsion phase was only detectable in the test tube experiments (Borji et al. 2022). This fact will be used in the following for the interpretation of core flooding results by means of cluster analysis and fractional pore occupation.

The actual performance of EOR systems is typically studied by classical continuum-scale core flooding experiments (Schumi, et al. 2020; Batenburg et al. 2015). Such measurements provide quantitative and robust data on oil recovery, but are insufficient when it comes to interpreting the reasons for high or low recovery. In this respect, pore-scale physics provides complementary and more detailed data;  $\mu\text{CT}$ -based core flow experiments for instance, provide access to microscopic distributions of fluid phases in the pore space and thus detailed information such as contact angle (Andrew et al. 2015; Scanziani et al. 2017), interfacial area and curvature (Armstrong et al. 2019; Berg et al. 2013), and fluid cluster sizes (Armstrong et al. 2019; Iglauer et al. 2010; Georgiadis et al. 2013; Rucker et al. 2019). Especially cluster size distribution has been linked to two-phase fluid mobility and fluid displacements (Armstrong et al. 2019; Andrew et al. 2023). Cluster length determines the mobility of ganglia at a given viscous pressure gradient and indicates whether a ganglion is trapped or mobile. This is directly relevant to EOR and can be expressed in a local capillary number for a single ganglion size (Armstrong et al. 2019) or calculated from a size distribution (Andrew et al. 2023). The size distribution usually follows a power law behavior with a lower limit determined by the pore size and a higher limit determined by the experimental field of view (Iglauer et al. 2010; Georgiadis et al. 2013). The power law indicates that there is no typical cluster size that could be used for mobility calculations. It has also been shown that the non-wetting phase is volumetrically dominated by a single large cluster (Georgiadis et al. 2013; Berg et al. 2015), which often forms a connected phase within the experimental field of view. However, most of these studies were conducted with idealized liquid systems (monomolecular, transparent, synthetic) such as decane brine or  $\text{CO}_2$  brine with relatively high interfacial tension, which also have well-defined wetting properties. These properties are not necessarily representative for crude oil brine systems. Pore-scale EOR experiments with crude oil are rarely performed. Examples of surfactant-flooding pore-scale experiments are given by Unsal et al. (2016); Broens and

Unsal 2018; Unsal et al. 2019; Alzahid et al. 2017; Alzahid et al. 2019; Kharrat et al. 2022) studying emulsification and its influence on displacement physics on the pore scale using idealized fluid systems. Pore-scale EOR experiments, including crude oil, are rather scarce and often focus on qualitative descriptions and recovery from the evaluation of saturation changes (Ott et al. 2020; Borji et al. 2022; Schumi et al. 2020). A detailed cluster analysis of an EOR system including crude oil was performed by Ott et al. (2020) in a 2D idealized microfluidic chip. In this study it was shown that an EOR potential can be derived from the cluster volume distribution using a Lorentz analysis.

While the analysis of cluster-size or cluster-volume distributions provide information on ganglion size, mobility and trapping, and fluid phase connectivity, it does not directly relate the fluid displacements to the rock structure. The question remains: from which class of pores do we recover oil by which process? This question addresses oil left behind by microscopic bypass effects and how it can be recovered by cEOR. By lowering the interfacial tension and the associated reduction in capillarity, additional pore sizes should be accessible to the injection water regardless of the wetting properties, resulting in additional oil recovery. This work performed water–oil displacement experiments by systematically increasing the alkali concentration, thereby modifying the interfacial tension between the aqueous and crude oil phases. The exact microscopic phase distribution on the pore scale was measured by in situ  $\mu$ CT scanning, and the segmented fluid phases were analyzed by (a) cluster-statistical analysis and (b) by saturation states of individual pores in relation to the pore size distribution. By analyzing the microscopic fluid state, we approach the following questions: (a) from which fraction of the pore space the extra oil is extracted, (b) the dominant cluster size in which the remaining oil is organized, and (c) what is explicitly different in the optimal composition of the injection water. For the last point, we formulate a hypothesis.

## 2 Materials and Methods

The methodology was previously reported by Borji et al. (2022) and is briefly described here.

### 2.1 Fluids

The crude oil sample was derived from the 16 TH reservoir of the Matzen oil field, Austria. The sample was characterized by a viscosity  $\mu = 80$  cP at 20 °C, a density  $\rho = 905$  kg/m<sup>3</sup> at 22 °C, and a high TAN of 1.5–1.78 mg KOH/g (Magzymov et al. 2021; Batenburg et al. 2015), which makes the field a suitable candidate for EOR by alkaline flooding. Detailed field data and oil composition, including saturates, aromatics, resins, and asphaltenes analysis, addressing other surface-active components, have been reported (Andrew et al. 2015; Scanziani et al. 2017; Armstrong et al. 2019). To increase the X-ray contrast to the aqueous phase, 7 wt% iododecane (98% purity, Sigma-Aldrich) was added. The influence of the X-ray doping agents was investigated and minimized on the basis of the qualitatively observed phase behavior in the X-ray microtomography ( $\mu$ CT) scans. The alkaline solutions for the water injection were prepared by adding sodium carbonate (Na<sub>2</sub>CO<sub>3</sub>) powder (Sigma-Aldrich) to deionized (DI) water. Sodium carbonate is one of the commonly used alkaline agents (Lake et al. 2014) used in previous studies and a candidate for field application (Ott et al. 2020; Magzymov et al. 2021; Schumi, et al. 2020). Sodium carbonate is a

rather weak alkaline agent (compared to NaOH) with the advantageous property that the pH does not strongly depend on the concentration (Lake et al. 2014). Thus, constant chemical conditions can be achieved during flooding. The solution was magnetically stirred for 10 h. The pH was measured using an electronic pH meter, as previously reported (Ott et al. 2020; Borji et al. 2022; Georgiadis et al. 2013). All experiments were performed at ambient pressure and temperature (22 °C) because all presented types of experiments could be performed under these conditions, ensuring absolute comparability.

## 2.2 Porous Media

The mini-core flood experiments were performed in a cylindrical mini plug with a 5 mm diameter and a 15 mm length, drilled from a Robuglass<sup>®</sup> sintered glass filter, representing a 3D porous medium. Such samples were used in earlier studies (Georgiadis et al. 2013; Berg et al. 2014) and are characterized by a high porosity ( $\phi = 0.35$ ) and permeability ( $K = 22 \pm 2 D$ , whereas  $1 D \approx 10^{-12} \text{ m}^2$ ). Pore diameters were in the range of 40–100  $\mu\text{m}$  (FWHM) and the pore volume distribution is given in the result section. The total pore volume (PV) was 107 mm<sup>3</sup>. This specific porous medium was chosen for three reasons: (a) the pore space is well resolvable in  $\mu\text{CT}$ , (b) it supports laminar flow conditions, and (c) it is made of borosilicate glass, which is the same material as the test tubes and microfluidic chips, which have been used to characterize phase behavior (Borji et al. 2022). In this work, and with respect to cluster statistics, the 3D core flooding results are compared to microfluidic experiment from Borji et al. (2022). The microfluidic chips were made of borosilicate glass. The pore structure is characterized by an etching depth of 20  $\mu\text{m}$  and a lateral 2D definition of the pores and pore throats. The lateral average pore size (diameter) is 280  $\mu\text{m}$ , with a distribution width (FWHM) of 200  $\mu\text{m}$ . Porosity and permeability were determined to be  $\phi = 0.57$  and  $K = 2.5 D$ , respectively. The total domain size is  $20 \times 10 \text{ mm}^2$  with a channel system at the inlet and outlet for fluid distribution and collection, respectively. Due to the open and highly permeable pore structure, the microfluidic chip is comparable to the 3D miniplug.

## 2.3 Flooding Experiments

The 3D mini plug was embedded in a Viton rubber sleeve placed in an X-ray transparent carbon-fiber-epoxy-based core holder. To mitigate the adverse effects of the rubber sleeve wetting conditions, the sample was wrapped in a single layer of aluminum foil. The core holder was mounted on the sample-manipulation stage of the  $\mu\text{CT}$  scanner (ProCon X-ray, CT ALPHA). High-precision VP-series pumps from Vindum Engineering, Inc. were used for fluid injection and pressure confinement. Three-way high-pressure valves (Swagelok) and PEEK tubes were used as connections and flow lines between the pump, core holder, and effluent collection vessel at the outlet. For preparation and presaturation purposes, a vacuum pump was installed on the downstream side of the flow loop. The oil was then injected under vacuum conditions using a Chemyx Fusion 200 syringe pump with a Hamilton glass syringe. The experiments were finally carried out in a vertical flooding geometry under ambient pressure and temperature conditions.  $\mu\text{CT}$  scans were performed at the same photon energy as for the phase-behavior experiments (Borji et al. 2022), with a voxel size of 4.5  $\mu\text{m}$ . For this purpose, the X-ray projections were reconstructed using XAid software. The  $\mu\text{CT}$  scans were acquired before and at the end of each water and alkali flooding experiment in a steady state. Analogous settings were chosen for the 2D microfluidics

experiments. However, unlike the core flooding experiments, the flooding geometry was horizontal and a Chemyx Fusion 200 syringe pump was used for fluid injection. The saturation state was determined by optical imaging using a Leica DMi8 microscope and a DMC2900 camera. The volumetric flow rates of the core flow and microfluidic experiments were set to 0.002 and 0.00016 ml/min, respectively. For more details on the microfluidic setup, see Ott et al. (2020), Borji et al. (2022), Kharrat et al. (2022), Hassannayebi et al. (2019).

## 2.4 Image Processing and Analysis

The flooding experiments were performed with in situ  $\mu$ CT monitoring of the saturation state on the pore scale. Processing, analyzes, and visualizations of the resulting 3D  $\mu$ CT images were performed using ImageJ FIJI and Avizo (Thermo Fisher Scientific, USA) software. The interactive learning and segmentation toolkit *ilastik* (Berg et al. 2019) was used for classification and segmentation of fluid phases. Figure 2 shows sample images of raw and segmented images. The workflow is explained as follows:

- Step 1: The reconstructed  $\mu$ CT images were registered on the initial image taken at  $S_o = 1$  using the ‘scale-invariant feature transform’ (SIFT) algorithm (Lowe 1999, 2004), followed by ‘nonlocal means denoising’ (Buades et al. 2005, 2008).
- Step 2: The initial state for each experiment was a fully oil-saturated sample, i.e.,  $S_o = 1$ . The grayscale contrast between the solid grains and the oil-filled pore space is shown in Fig. 2e and allowed reliable segmentation of the pore space since both components are well separated in the grayscale histogram (Borji et al. 2022).
- Step 3: The segmented solid phase (grains) was used as a mask and was removed from the subsequent scans taken after the displacement experiments; all further image analysis steps were performed on the fluid phases in the remaining pore space. Figure 2a–d shows pore scale images after water flooding (WF) and alkaline flooding (AF) indicating the fluid–fluid contrast enhanced by iododecane, the X-ray contrast agent.
- Step 4: Aqueous and oleic phases were identified and segmented for ultimate recovery calculations and cluster analysis (see result part). The characterization of emulsion phases was performed on the basis of grayscale histograms and is discussed in Borji et al. (2022).

## 2.5 Monitoring Individual Pore Saturation

While most pore-scale studies focus on the shape and distribution of fluid clusters and their cumulative volumes, here, we present a new aspect; we study the saturation state in individual pores as function of pore-size classes and link the fluid displacements to the pore volume distribution. For this, individual pores were separated and labeled by applying the inverted Chamfer distance map and subsequently a watershed algorithm to the pore space segmented image (Legland et al. 2016). Approximately 70,000 individual pores were identified in the observed volume (Fig. 2h). These pore-labeled images were used as a mask to inspect the number and saturation state of each labeled pore after each flooding experiments (Fig. 2i, j).

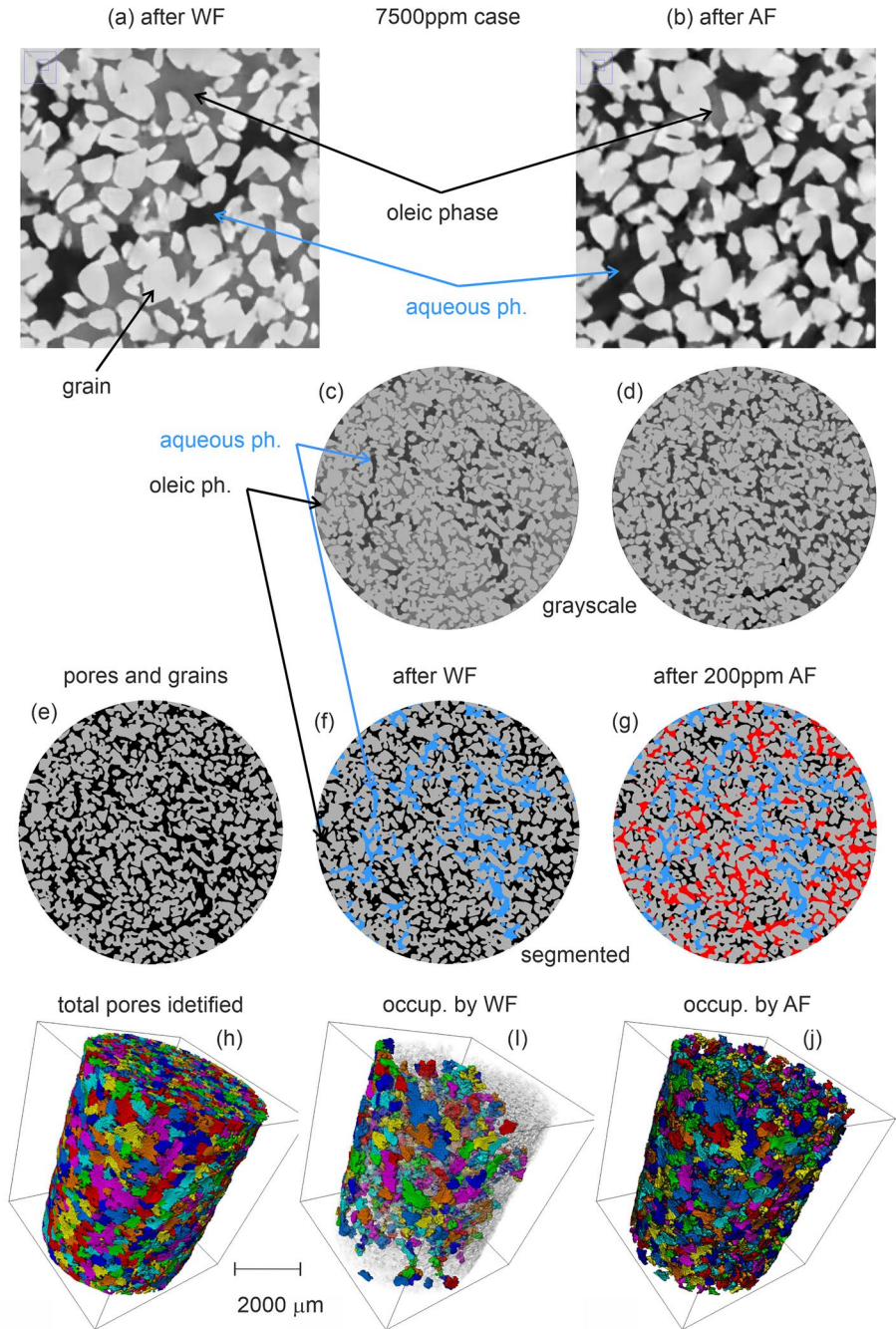


**Fig. 2** Pore-scale images after WF and AF. Top row: grayscale images after WF (a) and AF (b) of the 7500 ppm case. Second row: WF (c) and AF (d) of the 200 ppm case. Third row: segmented images of the 200-ppm case: e pore space, f water phase (blue) after WF, and g additionally displaced volume (red) after AF. Bottom row: h total identified pores displayed in different colors, i pore occupation after WF, and j after AF

### 3 Results and Discussion

#### 3.1 Emulsification Under Static and Dynamic Conditions

Following the phase-behavior experiments, the system under investigation (TH 16 crude) shows optimum behavior at a  $\text{Na}_2\text{CO}_3$  concentration of 7500 ppm. The optimum is thereby characterized by a minimum emulsion volume between the aqueous and oleic phases at the original oil–water contact (Winsor type III, Lake et al. 2014). Under dynamic conditions, the ultimate oil recovery in 2D microfluidics and 3D core flooding experiments shows at optimum  $\text{Na}_2\text{CO}_3$  concentration a maximum (Borji et al. 2022) in line with earlier core flood experiments (Schumi, et al. 2020). In the under-optimum the phase behavior showed extensive regions of loose emulsions (emulsions with large and widely distributed droplets) between the pure oil and water phases, as characterized by X-ray absorption measurements. When mixing the crude oil with pure water (0 ppm  $\text{Na}_2\text{CO}_3$ ), there is no evidence of emulsion formation. Above  $c_{\text{Na}_2\text{CO}_3} = 7500$  ppm, homogeneous oil-in-water emulsions below pure oil phases are detected. The oil-in-water content is below 10% up to 14,000 ppm. At 24,000 ppm, a single homogeneous emulsion phase is exhibited. The X-ray detected phase behavior is well reflected in the flooding experiments if additionally oil displacement is considered (Borji et al. 2022). Considering both the phase behavior and flooding experimental results, for  $\text{Na}_2\text{CO}_3$  concentrations that are not too high (excluding the 24,000 ppm case), relatively pure oil and water phases are expected and observed; those can be analyzed by cluster size distributions, as performed in earlier studies on generic systems with generic fluid phases, i.e., high-interfacial tension (IFT) systems (Georgiadis et al. 2013). With this assumption, we ignore the effects of phase swelling, which we estimate for the cases discussed in this work ( $c_{\text{Na}_2\text{CO}_3} \leq 12,000$  ppm) to be a maximum of 3 vol% at 12,000 ppm (Fig. 2c in Borji et al. 2022).

#### 3.2 Oil Cluster Analysis and EOR Potential

Figure 2 shows details of the image analysis workflow. The images were segmented into three clearly distinct phases indicated by the characteristic gray values (Fig. 2a–d): a solid phase, namely, the grains, an aqueous phase and a doped oleic phase. Slight grayscale variations inside the fluid phases indicate emulsification. These variations were explicitly studied in Borji et al. (2022) and were ignored in the present work. As Fig. 2a, b shows, even at the optimum condition of 7500 ppm  $\text{Na}_2\text{CO}_2$ , the oleic and aqueous phases are clearly distinguishable and can be segmented. Examples of the segmented images are shown in Fig. 2e–g. The binarized fluid phases can now be analyzed in a cluster-statistical way, as previously shown for high-IFT systems with generic fluid phases (Iglauer et al. 2010; Georgiadis et al. 2013; Berg et al. 2015). In microfluidics, it has been shown that a cluster-statistical analysis can also be applied to EOR systems to determine the EOR potential (Ott et al. 2020). In this study, a similar analysis was performed on the present EOR systems in 3D core flooding, and the results were compared to those from the same EOR system in the 2D microfluidics presented in Borji et al. (2022).

Figure 3 shows the cluster volume distributions (normalized frequency  $p(x)$ ) of all data sets (top panel) and after water flooding (WF) and subsequent alkaline flooding (AF) with 200 ppm and 7500 ppm  $c_{\text{Na}_2\text{CO}_3}$  in the panels below. As typically found in pore-scale investigations, the cluster distributions indicate for smaller clusters a straight line on the double



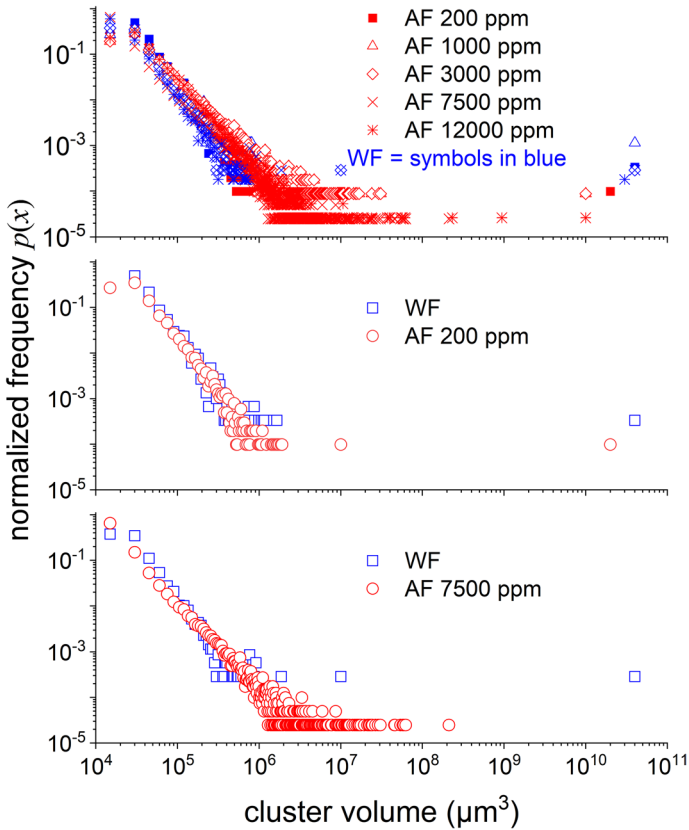
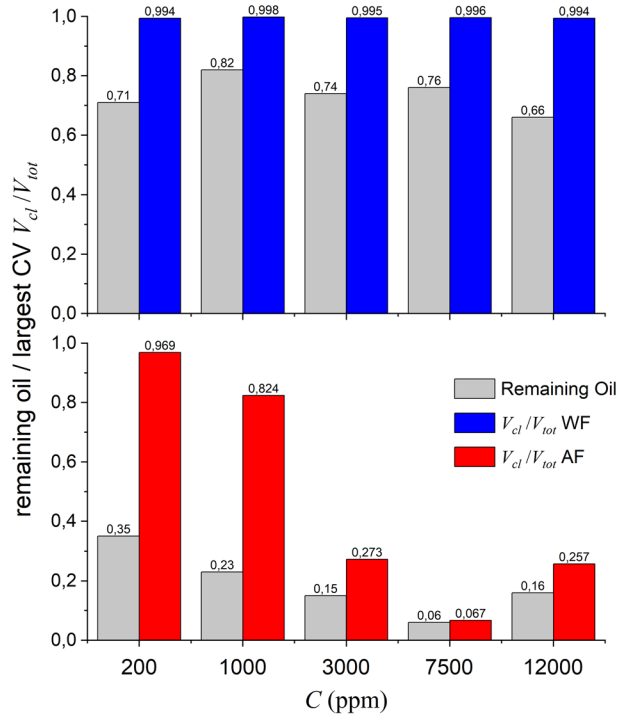


**Fig. 3** Oil cluster volume distributions after water flooding (blue, WF) and after alkaline flooding (red, AF); top: all data sets, middle: the 200 ppm case, and bottom: the 7500 ppm case

logarithmic plot and hence a power-law behavior; however, the overall saturation is dominated by a single large cluster, as also found in earlier studies (Georgiadis et al. 2013; Berg et al. 2015). After water flooding, in all cases, the residual oil is connected in a single cluster to more than 99% of its volume. Subsequent alkaline flooding breaks down larger clusters, leading to a wider power-law region tending toward a lower exponent (slope in the double logarithmic plot). The largest cluster still contained 97% and 7% of the total remaining oil volume for the 200 ppm and 7500 ppm cases, respectively. The closer the water composition is to the optimum alkaline concentration, the less the largest cluster dominates the oil saturation—the cluster size distribution became broader. Any tertiary recovery must therefore be related to an initially connected phase and the displacement and breakdown of this single dominating cluster.

The domination of the single largest cluster is shown in Fig. 4. The results show the remaining oil saturation after water flooding (top, gray bars) and subsequent alkaline flooding (bottom, gray bars) for different alkaline concentrations and the fraction of the largest cluster (blue (WF) and red (AF) bars). It is evident that at zero and low alkaline concentrations, the largest cluster dominates, while at alkaline concentrations above 1000 ppm  $c_{\text{Na}_2\text{CO}_3}$ , the largest cluster contributes only about 30% to 7% at optimum

**Fig. 4** Remaining oil saturation (gray bars) and the contribution of the largest cluster to the total remaining oil saturation after water flooding (blue bars) and alkaline flooding (red bars)



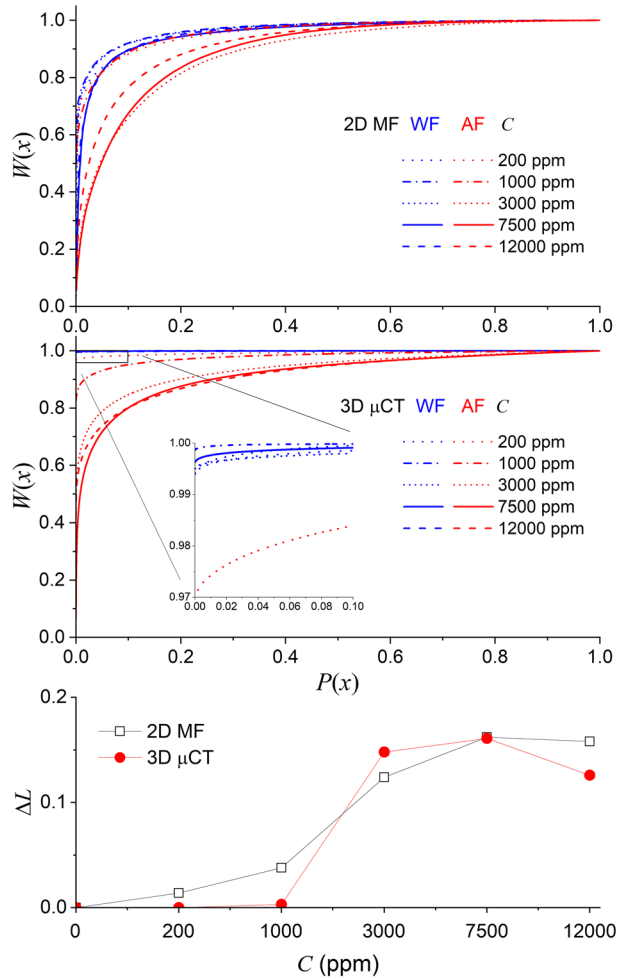
alkali concentrations. This is expected because the initial system (crude oil/DI water) has a relatively high interfacial tension (~ 16 mN/m), which can be lowered by the alkaline agent due to the relatively high TAN of the crude oil. This confirms the tendency as found in microfluidic experiments (Ott et al. 2020); however, the total volume fraction of the largest clusters did not exceed 50% in these experiments. This is expected due to the 2D nature of microfluidic porous media. 3D systems generally have a lower percolation threshold (Blunt 2017) due to their higher coordination number and bypassing possibilities.

In Ott et al. (2020), the EOR potential and optimum alkaline concentration were best reflected in the Lorenz analysis. This analysis not only considers large clusters but also the entire cluster size distribution in a cumulative way. The results appeared to be a good indicator of the imbalance of the cluster distribution, including the weight of the largest cluster in the system of investigation. However, it deals with relative distributions rather than with absolute volumes such as recovery factors and saturation. In a first step toward the Lorenz plot, we calculated the cumulative cluster volume distribution  $P(x)$  by integrating the cluster volume distribution  $p(x)$  from Fig. 3:

$$P(x) = \int_x^\infty p(y)dy.$$

In addition, we calculated the volume-weighted normalized cluster volume distribution ( $W(x)$ ) according to Ott et al. (2020):

**Fig. 5** Lorenz curves for WF (blue) and AF (red) from 2D microfluidic (MF, top) and 3D  $\mu$ CT-based core flooding (middle panel). The zoom-in highlights the variation in the individual 3D WF curves. Bottom panel: calculated Lorenz factors of 3D core floods and 2D microfluidics



$$W(x) = \frac{\int_x^\infty yp(y)dy}{\int_{x_{min}}^\infty yp(y)dy},$$

with  $x_{min}$  being the lower bound of the distribution. The  $W(P(x))$  results were plotted in the form of a Lorenz plot.

In Fig. 5, the resulting Lorenz plots are shown for two cases: the 3D core flood experiments (middle panel) and the 2D microfluidic experiments (top panel). Furthermore, we calculated the Lorenz factor, which provides the tendency toward smaller clusters, i.e., a measure of the EOR potential (Ott et al. 2020):

$$\Delta L = 2 \int_0^1 (W_{WF} - W_{AF})dP,$$

where  $WF$  and  $AF$  denote water flooding and alkaline flooding, respectively. In both types of experiments,  $\Delta L$  shows the same tendency in the 2D and 3D experiments; both show a

broad maximum at 7500 ppm, as shown in the bottom panel of Fig. 5. The largest cluster shows a minimum and no longer dominates oil saturation (Fig. 4). This is in line with the optimum displacement, which was previously identified on the basis of recovery and fluid phase behavior to be 7500 ppm (Borji et al. 2022). The characteristics indicate that (a) despite the different cluster volume distributions, the displacement characteristics in 2D and 3D are comparable and (b) the exact alkaline concentration is not very critical.

### 3.3 Characterization of Displacements by Pore Occupation

Thus far, we have analyzed and discussed oil clusters as typically performed in pore-scale investigations (Ott et al. 2020; Iglauer et al. 2010; Georgiadis et al. 2013). However, this approach does not adequately characterize displacement processes since the porous medium is not yet considered in terms of its pore size distribution. Under alkaline and surfactant flooding conditions the lowering of the IFT leading to a higher capillary number. By substantially lowering the capillary number different classes of pores can be accessed by the injection water and may be flooded. In the following, we analyzed the occupation of individual pores as function of pore sizes, assuming that pore sizes and pore throat sizes are correlated to each other. To analyze the pore occupation, we identified and labeled the individual pores and determined the respective saturation state from the segmented fluid phases, as described above. The result of this analysis is shown in Fig. 6. The top row shows the number frequency of flooded pores by WF (blue symbols) and AF (red symbols) as a function of pore size but irrespective of their saturation state. Both are compared to the total number frequency (black symbols). From panels (a) to (e), the alkali concentration

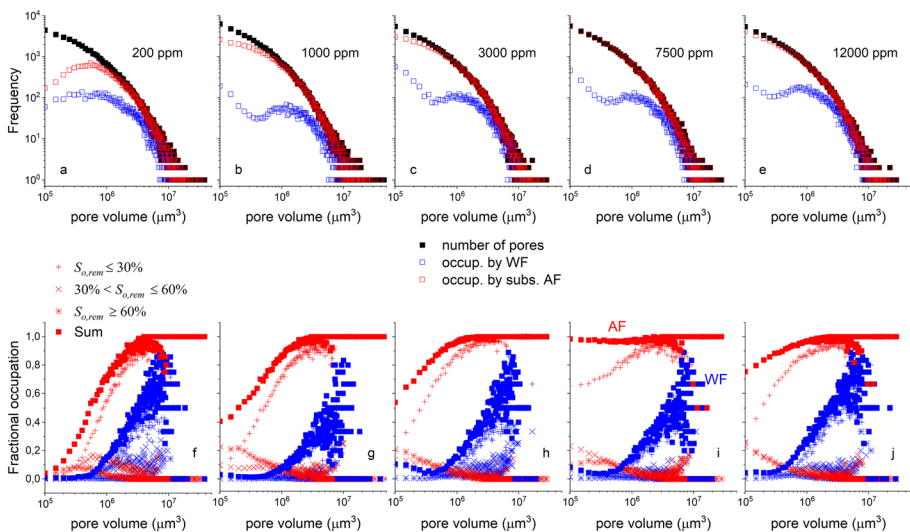


**Fig. 6** Top row **a–e** Number of pores (frequency) occupied by injected water as function of the (binned) pore volume; pore volume distribution (black) and pore occupation after water flooding (blue) and alkaline flooding (red). Panels **a–e** show the variation in the  $\text{Na}_2\text{CO}_3$  concentration from 200 ppm to 12,000 ppm. Bottom row **f–j** The blue and the red squares indicate the number of pores occupied by water and alkaline solution after water and alkaline flooding. Panels **f–j** show the variation in the  $\text{Na}_2\text{CO}_3$  concentration from 200 to 12,000 ppm. The crosses and stars show the fractional pore occupation according to the legend

increases from 200 to 12,000 ppm. All WF experiments show consistent behavior with a certain natural variation from experiment to experiment. The data show that during WF, predominantly larger pores are flooded. Smaller pores are penetrated to only a minor degree with pore volumes below  $10^6 \mu\text{m}^3$  being neglectable. Please note that the frequency is plotted on a logarithmic scale. This observation is in line with the observed oil-wet to mixed-wet behavior and the relatively high interfacial tension of  $\sim 16 \text{ mN/m}$  (Borji et al. 2022; Failed 2018), which makes the flow subject to local capillary forces. During the subsequent alkaline flooding, the larger pores appear entirely flooded, and the smaller pores become successively flooded with increasing alkaline concentration, or with decreasing IFT. Under optimum conditions, i.e., 7500 ppm  $c_{\text{Na}_2\text{CO}_3}$ , it can be observed that on the applied double logarithmic scale, all pores are occupied.

Since recovery is related to volumes and volumes are better represented on a linear scale, the lower row in Fig. 6 shows frequencies normalized by the pore size distribution on a linear scale. Therefore, this figure depicts the number fraction of occupied pores as a function of pore size. Furthermore, we would like to understand the respective saturation state,  $S_o$ , since the produced oil volume is related to the pore size times the water saturation in the respective pore. For practical reasons, we discriminated the saturation states in three categories with respect to the remaining oil saturation  $S_{o,\text{rem}}$  after WF and AF:  $S_{o,\text{rem}} \leq 30\%$ ,  $30\% < S_{o,\text{rem}} \leq 60\%$ , and  $S_{o,\text{rem}} > 60\%$ . Again, the alkaline concentration increases from left to right, i.e., from panels (f) to (j). Blue symbols correspond to WF and red symbols to AF. The crosses and stars correspond to the introduced categories, as indicated in the legend of the figure, i.e., the fractional occupation. The solid squares are the sums of these contributions and therefore correspond to the total flooded fraction of pores, represented in the upper row of Fig. 6. The WFs are all comparable with a certain natural variation. A first observation is that the largest pores are flooded and the majority of the WF pores are depleted to a high degree with a low remaining oil saturation. This is still true with increasing alkaline concentrations, but with the smaller pores being increasingly flooded with increasing alkaline concentration until the optimum is reached. Thereafter, the trend may be returned. Under optimum conditions, nearly all pores are flooded, as observed before on the logarithmic scale.

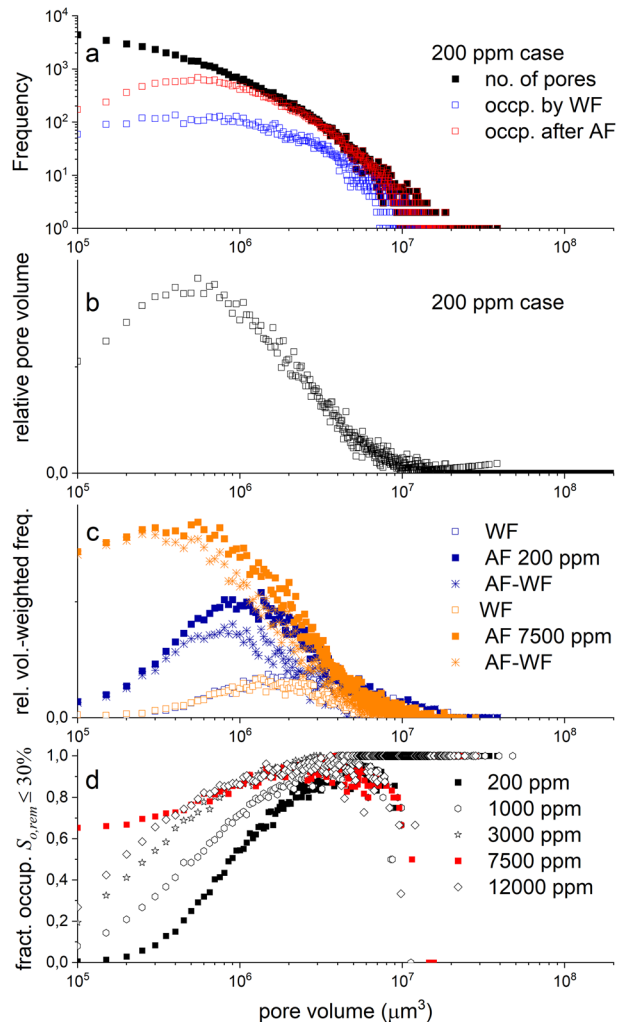
On the scale of a  $\mu\text{CT}$  field of view, the remaining oil saturation after water flooding is dominated by a single cluster or rather a connected oil phase to  $>99\%$ . The smaller clusters of Fig. 3 are practically irrelevant for enhanced oil recovery. After alkaline flooding, which reduces the interfacial tension, these clusters break down into smaller clusters. The largest cluster after AF under optimum conditions shows a size below 7% of the remaining oil volume (see Fig. 4), which corresponds to approximately 0.4% of the total observed pore volume. The cluster size is linked to the viscous force applied by injection water to the displaced phase. Smaller clusters potentially experience a smaller viscous force (by ignoring other parameters); i.e., the EOR potential decreases with cluster size during EOR displacements.

By analyzing fractional pore occupancy as a function of pore size, we obtain a different type of information, relating pore classes (within a cluster) to the oil produced. Therefore, by comparing the fractional occupation between initial water flooding and subsequent alkali flooding, information regarding the cluster's internal structure and the displacement process are given. After water flooding, on average, 74% of the oil remains in the observed sample volume, organized in a single large cluster. The oil in these clusters predominantly spans the fraction of smallest pores in the network. The system behaves similar to an oil-wet system (which may be a result of the  $S_{o,\text{in}} = 1$  starting conditions); i.e., the injected water predominantly invades the larger pores. However, in the majority of the water

flooded pores, the oil was displaced to a large extent with a relatively small amount of oil remaining ( $S_{o,rem} \leq 0.4$ ). This may be a result of the relatively large water interstitial velocity due to the relatively low cross section related to the low water saturation,  $S_w$ .

By subsequent alkaline flooding at 200 ppm, the oil was mobilized predominantly from pores with a volume of  $\sim 10^6 \mu\text{m}^3$  ( $2.7 \times 10^5$  to  $2.7 \times 10^6 \mu\text{m}^3$  FWHM, as shown in Fig. 7c). A fraction of the smaller pores in the network are invaded. The majority of the pore volume (see Fig. 7b) and the remaining oil are located in smaller pores with a volume of  $\sim 5 \times 10^5 \mu\text{m}^3$ . Therefore, additional oil recovery was limited to approximately 50% of the oil remaining after water flooding. The remaining oil is still organized in a single connected phase at  $S_o \sim 0.35$ . With increasing  $\text{Na}_2\text{CO}_3$  concentration, an increasingly larger fraction of the smaller and smallest pores is occupied, which is a sign of the successively reduced interfacial tension. When approaching optimum conditions, the oil is mobilized, where it is predominantly located in the pores, with an  $\sim 5 \times 10^5 \mu\text{m}^3$  volume (Fig. 7b, c). As seen in Fig. 6i and Fig. 7d, reaching optimum conditions results in not only a quantitative

**Fig. 7** Top panel **a** Pore volume distribution (number frequency) of the total pore space (black), the pores occupied by water after initial water flooding (blue), and the pores occupied after alkaline flooding with a 200 ppm  $\text{Na}_2\text{CO}_3$  solution. Panel **b** Relative pore volume—the number frequency times pore volume as a function of the pore volume. Panel **c** The number frequency weighted by the relative pore volume for WF and the subsequent 200 ppm and 7500 ppm AF. The difference between AF and WF shows the pore sizes from which additional oil was recovered. Panel **d** Number frequency of highly depleted pores for the different  $\text{Na}_2\text{CO}_3$  concentrations



improvement but also a qualitative change; the slope of the decay of highly depleted pores ( $S_{o,rem} \leq 0.3$ ) progresses toward smaller sizes. Considering this behavior together with the observation that the systems behave like oil-wet systems with high alkali solutions (Borji et al. 2022), a “close-to-miscible” displacement is indicated. In the absence of capillary forces, all classes of pores can be reached, even in an oil-wet state. As shown in Fig. 7d, at 12,000 ppm, the system falls back to the same trend (the same slope), i.e., below optimum.

## 4 Conclusions

We performed small-scale core flood experiments, displacing crude oil from the Vienna Basin by injecting water and  $\text{Na}_2\text{CO}_3$  alkaline solutions of different concentrations. The saturation scale was monitored by  $\mu\text{CT}$  imaging on the pore scale. Increasing alkaline concentrations led to enhanced oil recovery by saponification with acidic crude oil components. Ignoring details in emulsification and segmenting the aqueous and oleic phases in a binary way, we performed a cluster statistical analysis on the remaining oil clusters. Furthermore, we developed a new approach for analyzing the pore occupation and the remaining oil saturation in individual pores on a statistical basis.

From the analysis of the cluster size distribution, we found that after water flooding, the remaining oil is dominated by a single connected oil cluster, which spans the total observed domain, containing  $>99\%$  of the remaining oil, appearing as a connected phase. By subsequent alkali flooding, these clusters break down to smaller clusters until the optimum alkali concentration of 7500 ppm  $c_{\text{Na}_2\text{CO}_3}$  is reached. Under optimum conditions, the volume of the largest cluster is  $<7\%$ , which is approximately  $0.4\%$  of the total observed pore volume. Since the largest cluster is no longer dominant, the exact cluster size distribution matters. We link the cluster size distribution to an EOR potential via the Lorenz factor (Ott et al. 2020). It shows the tendency of oil cluster toward a more uniform size distribution toward optimal alkali concentration.

The analysis of pore-occupation distributions, i.e., the saturation states of pores as a function of pore size, provides deeper insight into the nature of the water–oil displacement processes and their variation as a function of alkali concentration, i.e., mobilization potential of in situ surfactants. Furthermore, despite demonstrating signatures of two-phase displacements with distinctly separated fluid phases in phase-behavior experiments (Borji et al. 2022) and during displacement, at optimum alkali concentration, the displacement shows the efficiency and characteristics of a purely miscible displacement. Under optimum conditions, the injection water displaces oil from all sizes of pores with a pore-occupation distribution that is qualitatively different from the other cases. The further away from the optimum, the smaller fractions of pores of the initially oil-wet system are less reachable, which is a signature of finite capillarity, i.e., a finite IFT.

From these observations, we can formulate our hypothesis. The reduction in the interfacial tension has two effects: First, the large oil cluster breaks down into smaller clusters. This is possible because the lower interfacial tension allows the formation of fluid–fluid interfaces without much energy input. However, due to the negligible interfacial tension, the smaller clusters formed remain mobile and can be displaced. In addition, the negligible interfacial tension results in the ability to flood smaller pores as capillary boundaries are eliminated. Both effects lead to additional oil production. The question remains as to the optimum displacement or optimum  $\text{Na}_2\text{CO}_3$  concentration. Let us assume that the interfacial tension is lowest at the optimum concentration and that almost miscible displacement

occurs. Under these conditions, the oil is displaced on first contact with the injection water. At less ideal displacement, as can be assumed outside the optimum, the oil is less well mobilized and therefore has longer contact with the injection water. Multiple contacts lead to emulsion formation and hence entrapment. This last mechanism cannot be demonstrated within the scope of this work, but may be evident from the microfluidic experiments and discussions in Borji et al. (2022).

The study showed that pore-scale investigation provides rich data sets compared to classical phase behavior and coreflooding experiments. Direct and visual insights into pore-scale displacements allow for a better understanding of displacement physics and therefore allow for an educated and targeted design of chemical-water composition. With the present work, the literature on pore-scale physics is extended in two directions. (a) Since, literature on complex fluid systems is scarce, pore-scale physics remains academic. Thus, the present work combines detailed insights and applications in view of the similar future developments. (b) The fractional pore occupation provides a simple but novel method to better understand and quantify the role of capillarity barriers in fluid displacement and thus the volume from which oil is recovered. In combination with cluster analysis and, more specifically, the Lorenz analysis, the EOR potential of a system can be determined.

**Acknowledgements** This work was partly performed in the frame of the EmulPore project funded by the Austrian Research Promotion Agency (FFG), with the OMV Exploration & Production GmbH as a project partner. The authors would like to acknowledge Pit Arnold for his experimental support and valuable discussions.

**Funding** Open access funding provided by Montanuniversität Leoben.

**Open Access** This article is licensed under a Creative Commons Attribution 4.0 International License, which permits use, sharing, adaptation, distribution and reproduction in any medium or format, as long as you give appropriate credit to the original author(s) and the source, provide a link to the Creative Commons licence, and indicate if changes were made. The images or other third party material in this article are included in the article's Creative Commons licence, unless indicated otherwise in a credit line to the material. If material is not included in the article's Creative Commons licence and your intended use is not permitted by statutory regulation or exceeds the permitted use, you will need to obtain permission directly from the copyright holder. To view a copy of this licence, visit <http://creativecommons.org/licenses/by/4.0/>.

## References

- Ahmed, T., Meehan, D.N.: Chapter 6 - Introduction to Enhanced Oil Recovery, pp. 541–585. Gulf Professional Publishing, Boston (2012)
- Alzahid, Y.A., Mostaghimi, P., Walsh, S.D.C., Armstrong, R.T.: Flow regimes during surfactant flooding: The influence of phase behaviour. *Fuel* **236**, 851–860 (2019)
- Alzahid, Y., Mostaghimi, P., Warkiani, M.E., Armstrong, R.T., Joekar-Niasar, V., Karadimitriou, N.: Alkaline surfactant polymer flooding: What happens at the pore scale? In: SPE Europec featured at EAGE Conference and Exhibition? SPE, p. D022S014R003 (2017)
- Amaya, J., Rana, D., Hornof, V.: Dynamic interfacial tension behavior of water/oil systems containing in situ-formed surfactants. *J. Solut. Chem.* **31**(2), 139–148 (2002)
- Andrew, M., Bijeljic, B., Blunt, M.J.: Pore-by-pore capillary pressure measurements using X-ray microtomography at reservoir conditions: curvature, snap-off, and remobilization of residual CO<sub>2</sub>. *Water Resour. Res.* **50**(11), 8760–8774 (2014)
- Andrew, M., Menke, H., Blunt, M.J., Bijeljic, B.: The imaging of dynamic multiphase fluid flow using synchrotron-based X-ray microtomography at reservoir conditions. *Transp. Porous Media* **110**(1), 1–24 (2015)
- Annual Energy Outlook: ed. [https://www.eia.gov/outlooks/aeo/pdf/AEO2023\\_Narrative.pdf](https://www.eia.gov/outlooks/aeo/pdf/AEO2023_Narrative.pdf): U.S. Energy Information Administration (EIA) (2023)



- Armstrong, R.T., Georgiadis, A., Ott, H., Klemin, D., Berg, S.: Critical capillary number: desaturation studied with fast X-ray computed microtomography. *Geophys. Res. Lett.* **41**(1), 55–60 (2014). <https://doi.org/10.1002/2013GL058075>
- Arnold, P.: Experimental investigation of interfacial tension for alkaline flooding. University of Leoben, Leoben (2018)
- Berg, S., et al.: Real-time 3D imaging of Haines jumps in porous media flow. *Proc. Natl. Acad. Sci.* **110**(10), 3755 (2013). <https://doi.org/10.1073/pnas.1221373110>
- Berg, S., et al.: Multiphase flow in porous rock imaged under dynamic flow conditions with fast X-ray computed microtomography. *Petrophysics* **55**(04), 304–312 (2014)
- Berg, S., et al.: Onset of oil mobilization and nonwetting-phase cluster-size distribution. *Petrophysics* **56**(01), 15–22 (2015)
- Berg, S., et al.: ilastik: Interactive machine learning for (bio)image analysis. *Nat. Methods* **16**(12), 1226–1232 (2019)
- Blunt, M.J.: *Multiphase Flow in Permeable Media: A Pore-Scale Perspective*. Cambridge University Press, Cambridge (2017)
- Borji, M., Kharrat, A., Ott, H.: Comparability of in situ crude oil emulsification in phase equilibrium and under porous-media-flow conditions. *J. Colloid Interface Sci.* **615**, 196–205 (2022). <https://doi.org/10.1016/j.jcis.2022.01.182>
- Broens, M., Unsal, E.: Emulsification kinetics during quasi-miscible flow in dead-end pores. *Adv. Water Resour.* **113**, 13–22 (2018)
- Buades, A., Coll, B., Morel, J.-M.: Nonlocal image and movie denoising. *Int. J. Comput. vis.* **76**(2), 123–139 (2008)
- Buades, A., Coll, B., Morel, J.-M.: A non-local algorithm for image denoising. In: 2005 IEEE Computer Society Conference on Computer Vision and Pattern Recognition (CVPR'05), vol 2, pp. 60–65. IEEE (2005)
- Chatterjee, J.: A novel mechanism of dynamic interfacial tension reduction in triglyceride-alkaline aqueous solution system. *Colloids Surf. A* **204**(1), 93–102 (2002)
- Cooke, C.E., Jr., Williams, R.E., Kolodzie, P.A.: Oil recovery by alkaline waterflooding. *J. Pet. Technol.* **26**(12), 1365–1374 (1974). <https://doi.org/10.2118/4739-pa>
- Ding, M., Wang, Y., Yuan, F., Zhao, H., Li, Z.: A comparative study of the mechanism and performance of surfactant- and alkali-polymer flooding in heavy-oil recovery. *Chem. Eng. Sci.* **219**, 115603 (2020)
- Georgiadis, A., Berg, S., Makurat, A., Maitland, G., Ott, H.: Pore-scale micro-computed-tomography imaging: Nonwetting-phase cluster-size distribution during drainage and imbibition. *Phys. Rev. E* **88**(3), 033002 (2013). <https://doi.org/10.1103/PhysRevE.88.033002>
- Green, D.W. and Willhite, G.P.: *Enhanced Oil Recovery*. Henry L. Doherty Memorial Fund of AIME, Society of Petroleum Engineers (1998)
- Hassannayebi, N., Azizmohammadi, S., De Lucia, M., Ott, H.: Underground hydrogen storage: application of geochemical modelling in a case study in the Molasse Basin, Upper Austria. *Environ. Earth Sci.* **78**(5), 177 (2019). <https://doi.org/10.1007/s12665-019-8184-5>
- Hemmati-Sarapardeh, A., Schaffie, M., Ranjbar, M., Dong, M., Li, Z.: *Chemical Methods*. Gulf Professional Publishing, Houston (2021)
- Iglauer, S., Favretto, S., Spinelli, G., Schena, G., Blunt, M.J.: X-ray tomography measurements of power-law cluster size distributions for the nonwetting phase in sandstones. *Phys. Rev. E* **82**(5), 056315 (2010)
- Johnson, C.E., Jr.: Status of caustic and emulsion methods. *J. Pet. Technol.* **28**(01), 85–92 (1976)
- Kharrat, A., et al.: Development of foam-like emulsion phases in porous media flow. *J. Colloid Interface Sci.* **608**, 1064–1073 (2022). <https://doi.org/10.1016/j.jcis.2021.10.022>
- Khlaifait, A.L., Dakhllallah, D., Sufyan, F.: A critical review of alkaline flooding: mechanism, hybrid flooding methods, laboratory work, pilot projects, and field applications. *Energies* **15**(10), 3820 (2022)
- Lake, L.W., Johns, R., Rossen, B., Pope, G.A.: *Fundamentals of Enhanced Oil Recovery*. Society of Petroleum Engineers, London (2014)
- Legland, D., Arganda-Carreras, I., Andrey, P.: MorphoLibJ: integrated library and plugins for mathematical morphology with ImageJ. *Bioinformatics* **32**(22), 3532–3534 (2016)
- Lowe, D.G.: Distinctive image features from scale-invariant keypoints. *Int. J. Comput. vis.* **60**(2), 91–110 (2004)
- Lowe, D.G.: Object recognition from local scale-invariant features. In: *Proceedings of the Seventh IEEE International Conference on Computer Vision*, vol. 2, pp. 1150–1157. IEEE (1999)
- Magzymov, D., Clemens, T., Schumi, B., Johns, R.T.: Experimental analysis of alkali-brine-alcohol phase behavior with high acid number crude oil. *SPE Reserv. Evaluation Eng.* **24**(02), 390–408 (2021)
- Nourani, M. et al.: Chapter 5 - alkaline-surfactant polymer (ASP). In: *Enhanced Oil Recovery Series*. Gulf Professional Publishing, Houston, pp. 221–247 (2022)

- Oil 2023: ed. <https://www.iea.org/reports/oil-2023>: International Energy Agency (2023)
- Ott, H., Kharrat, A., Borji, M., Arnold, P.: Fluid-phase topology of complex displacements in porous media. *Phys. Rev. Res.* **2**(2), 023240 (2020). <https://doi.org/10.1103/PhysRevResearch.2.023240>
- Rücker, M., et al.: From connected pathway flow to ganglion dynamics. *Geophys. Res. Lett.* **42**(10), 3888–3894 (2015). <https://doi.org/10.1002/2015GL064007>
- Saha, R., Uppaluri, R.V.S., Tiwari, P.: Influence of emulsification, interfacial tension, wettability alteration and saponification on residual oil recovery by alkali flooding. *J. Ind. Eng. Chem.* **59**, 286–296 (2018)
- Scanziani, A., Singh, K., Blunt, M.J., Guadagnini, A.: Automatic method for estimation of in situ effective contact angle from X-ray micro tomography images of two-phase flow in porous media. *J. Colloid Interface Sci.* **496**, 51–59 (2017)
- Schumi, B., et al.: Alkali/cosolvent/polymer flooding of high-TAN oil: using phase experiments, micromodels, and corefloods for injection-agent selection. *SPE Reserv. Eval. Eng.* **23**(02), 463–478 (2020)
- She, Y., et al.: Pore-scale study of in-situ surfactant flooding with strong oil emulsification in sandstone based on X-ray microtomography. *J. Ind. Eng. Chem.* **98**, 247–261 (2021)
- Sheng, J.J.: *Modern Chemical Enhanced Oil Recovery: Theory and Practice*. Gulf Professional Publishing, Houston (2010)
- Sheng, J.J.: *Enhanced Oil Recovery Field Case Studies*. Gulf Professional Publishing, Houston (2013)
- Stoll, W.M., et al.: Alkaline/surfactant/polymer flood: from the laboratory to the field. *SPE Reserv. Eval. Eng.* **14**(06), 702–712 (2011)
- Tagavifar, M., Xu, K., Jang, S.H., Balhoff, M.T., Pope, G.A.: Spontaneous and flow-driven interfacial phase change: dynamics of microemulsion formation at the pore scale. *Langmuir* **33**(45), 13077–13086 (2017)
- Tang, M., et al.: Investigation into the mechanisms of heavy oil recovery by novel alkaline flooding. *Colloids Surf. A* **421**, 91–100 (2013). <https://doi.org/10.1016/j.colsurfa.2012.12.055>
- Unsal, E., Broens, M., Armstrong, R.T.: Pore scale dynamics of microemulsion formation. *Langmuir* **32**(28), 7096–7108 (2016)
- Unsal, E., Rücker, M., Berg, S., Bartels, W.B., Bonnin, A.: Imaging of compositional gradients during in situ emulsification using X-ray micro-tomography. *J. Colloid Interface Sci.* **550**, 159–169 (2019)
- van Batenburg, D.W., Berg, S., Oedai, S., Elewaut, K.: Visualization of oil mobilization in ASP core floods using X-ray CT imaging. In: *SPE Kuwait Oil and Gas Show and Conference*, p. SPE-175407-MS (2015)
- de Zabala, E.F., Vislocky, J.M., Rubin, E., Radke, C.J.: A chemical theory for linear alkaline flooding. *Soc. Pet. Eng. J.* **22**(02), 245–258 (1982)
- Zhao, X., Feng, Y., Liao, G., Liu, W.: Visualizing in-situ emulsification in porous media during surfactant flooding: a microfluidic study. *J. Colloid Interface Sci.* **578**, 629–640 (2020)

**Publisher's Note** Springer Nature remains neutral with regard to jurisdictional claims in published maps and institutional affiliations.